Electromagnetically-Induced-Absorption-Mediated Ultrahigh-Rejection Microwave Photonic Notch Filter Using Single-Sideband Modulation

Varun M.K. and Ravi Pant*

Laboratory for Phoxonics and Nonlinear Optics in Nanostructures (PHONON), School of Physics, Indian Institute of Science Education and Research (IISER), Thiruvananthapuram, Kerala 695551, India

(Received 2 June 2021; revised 6 August 2021; accepted 9 August 2021; published 27 August 2021)

The inherent narrow bandwidth and wavelength-transparent nature of the stimulated Brillouin scattering (SBS) process make it a potential candidate for high-resolution wideband microwave photonic notch filters (MPNFs). The simplest way to realize a SBS-based MPNF is to use the narrowband Brillouin loss resonance with single-sideband modulation, where the modulation sideband is at the anti-Stokes frequency. However, using Brillouin loss with single-sideband modulation is highly inefficient because a large notch extinction requires large Brillouin loss, and thus, a large pump power. Here, we exploit an analogue of electromagnetically induced absorption (EIA) in the microwave domain to enhance MPNF rejection, at a fixed Brillouin pump power, by more than 6 orders of magnitude. We use this analogue of EIA to realize a MPNF with $>$ 75-dB rejection up to 40 GHz, using a Brillouin loss of about 15 dB. We harness a coherent Brillouin interaction between the orthogonally polarized components of a probe, which is comprised of a laser carrier and a single-modulation sideband. Stimulated Brillouin scattering and other components used in our demonstration have recently been demonstrated on integrated platforms. The proposed scheme, therefore, has the potential for realizing efficient integrated microwave photonic notch filters with ultrahigh rejection.

DOI: 10.1103/PhysRevApplied.16.024053

I. INTRODUCTION

Microwave photonic notch filters (MPNFs), which are an indispensable component of a microwave photonic signal processor [1–6], provide an attractive way to selectively filter out the unwanted radio-frequency interferers in applications such as radio-over-fiber communication and radar ranging [7–12]. Wide tunability, large extinction, bandwidth reconfigurability, immunity from electromagnetic interference, and ease of integration with existing optical communication systems make them desirable over electronic filters. Over the past decade, there have been several demonstrations of microwave photonic notch filters using optical delay lines [13–17], microresonators [18–26], a Sagnac loop [27,28], a phase-modulator-incorporated Lyot filter [29], fiber Bragg gratings [30], and Kerr microcombs [31]. While wide tunability has been achieved using these techniques, realizing high resolution with a large extinction is challenging.

Stimulated Brillouin scattering is an inelastic scattering process, which occurs due to an interaction between a strong optical pump wave (ω_{pump}), a weak optical probe wave (ω_{probe}), and an acoustic wave of frequency Ω_B in a nonlinear optical medium [32–36]. When the probe signal has a lower frequency than the pump ($\omega_{\text{probe}} = \omega_{\text{pump}} - \Omega_B$), the process is termed as Stokes scattering. For Stokes scattering, the pump is annihilated to create an acoustic phonon and a photon at the probe frequency, which results in the appearance of a gain resonance at the probe's (Stokes') signal frequency. If the probe frequency is higher than the pump frequency by the Brillouin frequency ($\omega_{\text{probe}} = \omega_{\text{pump}} + \Omega_B$), the process is then called anti-Stokes scattering. For anti-Stokes scattering, the probe photon creates a photon at the pump frequency and generates an acoustic phonon, which results in a loss of the probe photon and the appearance of a Brillouin loss resonance at the anti-Stokes frequency. In Stokes and anti-Stokes scattering, energy and momentum remain conserved [32,33]. For a given medium, the linewidth ($\Gamma_B = 1/\tau_{\text{acoustic}}$) of the Brillouin gain and loss resonance associated with the Stokes and anti-Stokes signals depends on the acoustic phonon lifetime, τ_{acoustic}. For a single-mode silica optical fiber, $\tau_{\text{acoustic}} \sim 10.6$ ns, which results in a full width at half maximum (FWHM) linewidth of $\Gamma_B/\pi \sim 30$ MHz. The narrow bandwidth of the stimulated Brillouin scattering (SBS) gain and loss resonance makes it a promising candidate for high-resolution microwave photonic bandpass [37–45] or band-reject filters [41,46–53].

*rpant@iisertvm.ac.in

SBS-based notch filters either use single-sideband modulation (SSB) in combination with Brillouin loss [46] or combine rf interference with double-sideband (DSB) modulation, where one of the modulation sidebands is processed with Brillouin gain and/or loss resonance [43,47,48,50,53–55]. A MPNF based on SSB modulation and SBS loss resonance is highly inefficient, as the rejection depth is in the order of the Brillouin loss. So, a MPNF with 60-dB rejection requires a Brillouin loss of 60 dB, and therefore, a large Brillouin pump power [46]. Furthermore, a higher Brillouin loss results in a larger 3-dB bandwidth, and thus, in reduced resolution. The rf-interference-based SBS MPNF, on the other hand, is highly efficient, as it exploits destructive interference between two rf signals, which results from the beating of a carrier with upper and lower modulation sidebands generated using DSB modulation. An interference-based MPNF uses unequal-amplitude-modulation sidebands with π phase difference between them. Processing of the modulation sidebands with SBS gain and/or loss equalizes the amplitudes of the interfering rf signals at the desired notch frequency. The presence of the π phase difference between the two rf signals then results in the appearance of a large rejection band at a frequency where their amplitudes are equalized through SBS processing. However, the presence of dispersion causes the phase difference between the interfering rf signals to deviate from π [56], which results in a large reduction in the rejection depth. A larger rejection-depth penalty is expected for higher radio frequencies, as the two modulation sidebands are separated by twice the modulation frequency.

Here, we propose a microwave photonic notch filter based on an analogue of electromagnetically induced absorption (EIA) in the microwave domain [57]. Electromagnetically induced absorption, which results due to interference between different excitation pathways, enhances the absorption of an already existing absorption resonance [58–61]. We harness destructive interference between the Brillouin loss resonances in the microwave domain, which are created by beating of the carrier in orthogonal polarizations with the anti-Stokes sideband in the respective polarization, to enhance the loss at a desired microwave frequency by more than 6 orders of magnitude at a fixed pump power. Combining single-sideband modulation with polarization-dependent Brillouin loss and bias-voltage-induced phase allows us to achieve a MPNF with an ultrahigh rejection of > 75 dB and a narrow 3-dB bandwidth of (77 ± 7) MHz using about 15 dB of SBS loss. The proposed notch filter is tunable over 40 GHz with minimum rf loss of 17.5 dB at 10 GHz. Over the entire tuning range up to 40 GHz, the MPNF exhibits rf loss of (-22.9 ± 5.4) dB. To study the effectiveness of our scheme, we selectively suppress an interferer, which is 25 dB stronger than the desired rf signal, by 51 dB without affecting the rf signal.

II. THEORY

We exploit the polarization dependence of SBS loss seen by the orthogonally polarized components of the anti-Stokes sideband and combine it with the polarization dependence of the bias-voltage-induced phase to enhance loss at a desired microwave frequency. Figure 1 shows a schematic representation of the concept of an EIA-based MPNF. An optical carrier of frequency ω_c (Fig. 1, node a) is modulated with a radio-frequency ($\Omega_{\rm rf}$) signal, using a z-cut intensity modulator (IM), to generate the upper and lower modulation sidebands at $\omega_c \pm \Omega_{\rm rf}$ (see Fig. 1, node b). The z-cut IM is based on a lithium niobate waveguide, where the phase shift of the upper and lower modulation sidebands with respect to the carrier depends on the IM bias voltage, V_b, through a parameter α. The parameter α shifts the phases of the sidebands by $\pm\tan^{-1}\alpha$ [53]. A z-cut intensity modulator also shows a polarization dependence of the bias-induced phase shift due to different electro-optic coefficients of the extraordinary ($r_e = 30.8$ pm/V) and ordinary ($r_o = 8.6$ pm/V) polarization components perpendicular to the light-propagation direction in the modulator. Considering small signal modulation, the resulting electric field at the output of a z-cut IM for probe components along two orthogonal polarizations is then given as [57]

$$\begin{aligned} E(t) = {} & \frac{E_{0x}}{2} e^{i\omega_c t}\, e^{i\phi_{0x}} [2\cos\Delta\phi_{0x} \\ & + \frac{m_x V_0 \sin\Delta\phi_{0x}}{2}(1 + i\alpha_x)(e^{i\Omega_{\rm rf}t} + e^{-i\Omega_{\rm rf}t})] \\ & + \frac{E_{0y}}{2} e^{i\omega_c t} \sin e^{i\phi_{0y}} [2\cos\Delta\phi_{0y} \\ & + \frac{m_y V_0 \sin\Delta\phi_{0y}}{2}(1 + i\alpha_y)(e^{i\Omega_{\rm rf}t} + e^{-i\Omega_{\rm rf}t})], \end{aligned} \quad (1)$$

where $\Delta\phi_{0x,0y} = \phi_{01x,01y} - \phi_{02x,02y}/2$ and $\phi_{0x,0y} = \phi_{01x,01y} + \phi_{02x,02y}/2$, with $\phi_{01x,01y}$ and $\phi_{02x,02y}$ being the bias-dependent phase shifts in the two arms of a z-cut intensity modulator for the x and y polarizations. The parameter $m_{x,y} = m_{2x,2y} - m_{1x,1y}$ depends on the modulation parameters $m_{1x,1y}$ and $m_{2x,2y}$ in the two arms of the intensity modulator. V_0 is the rf voltage of the modulation signal. $E_{0x,0y}$ are electric fields along the orthogonal polarization components of the signal. For a z-cut intensity modulator, the parameter $\alpha_{x,y}$ can be defined as

$$\alpha_{x,y} = -\frac{m_{1x,1y} + m_{2x,2y}}{m_{1x,1y} - m_{2x,2y}} \cot(\Delta\phi_{0x,0y}). \quad (2)$$

Here, $\Delta\phi_{0x,0y}$ can be controlled by tuning the bias voltage, V_b, which allows electrical control of the phase shift [62,63]. After modulation, one of the sidebands ($\omega_c + \Omega_{\rm rf}$) is filtered out using a narrowband optical filter to create a probe with a single-modulation sideband ($\omega_c - \Omega_{\rm rf}$) and

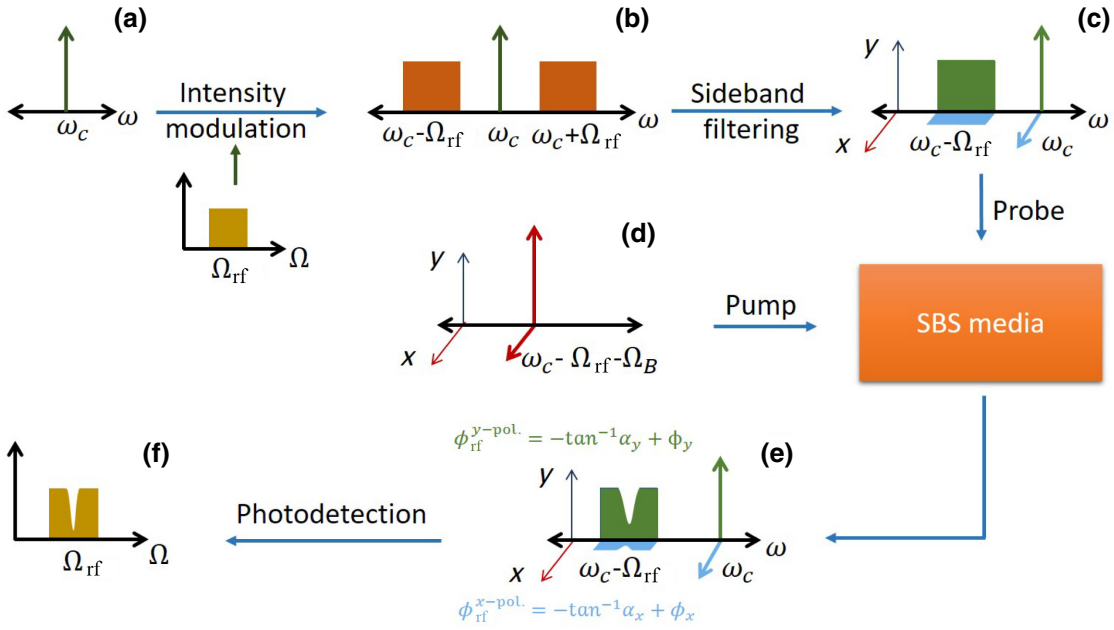

FIG. 1. Schematic representation of the concept of EIA-based MPNF. Node a, modulation of laser carrier of frequency ω_c by Ω_{rf}; node b, upper and lower sidebands generated at intensity modulator of $\omega_c - \Omega_{rf}$ and $\omega_c + \Omega_{rf}$, respectively; node c, optical filtering of upper sideband to create a probe consisting of a lower sideband and carrier with different power distributions in orthogonal polarization components; node d, optical pump centered at frequency $\omega_c - \Omega_{rf} - \Omega_B$ with different power distributions in orthogonal polarization components; node e, back-scattered probe on interaction with pump; amplitude of orthogonal polarization components of probe signal are equal at desired rf frequency (Ω_{rf}); node f, photodetection of different losses witnessed by orthogonal polarization components of lower sideband.

a carrier. By tuning probe polarization, the power in one of the orthogonal polarization (x-pol) components can be made smaller than that in the other polarization component (y-pol), as shown in Fig. 1, node c. After filtering the modulation sideband at $\omega_c + \Omega_{rf}$, the optical probe in Eq. (1) can be written as

$$\begin{aligned} E(t) = {} & \frac{E_{0x}}{2} e^{i\omega_c t}\, e^{i\phi_{0x}} [2\cos\Delta\phi_{0x} \\ & + \frac{m_x V_0 \sin\Delta\phi_{0x}}{2} \sqrt{1+\alpha_x^2}\, e^{-i(\Omega_{rf} t + \tan^{-1}\alpha_x)}] \\ & + \frac{E_{0y}}{2} e^{i\omega_c t}\, e^{i\phi_{0y}} [2\cos\Delta\phi_{0y} \\ & + \frac{m_y V_0 \sin\Delta\phi_{0y}}{2} \sqrt{1+\alpha_y^2}\, e^{-i(\Omega_{rf} t + \tan^{-1}\alpha_y)}]. \end{aligned} \quad (3)$$

We use a backward SBS in an optical fiber to realize EIA. Light from an another laser centered at a frequency of $\omega_p = \omega_c - \Omega_{rf} - \Omega_B$ is used as the Brillouin pump (Fig. 1, node d). When the probe is counterpropagated to a Brillouin pump in a SBS medium, different polarization components of the probe sideband will see different Brillouin losses, depending on the pump power along the orthogonal polarizations [57] (see Fig. 1, node e). By tuning the pump polarization, the pump power distribution along two orthogonal polarization components is altered to impart different SBS losses on the corresponding anti-Stokes components. The resulting electric field of the probe signal can then be written as [57]

$$\begin{aligned} E(t) = {} & \frac{E_{0x}}{2} e^{i\omega_c t}\, e^{i\phi_{0x}} [2\cos\Delta\phi_{0x} \\ & + \frac{m_x V_0 \sin\Delta\phi_{0x}}{2} \sqrt{1+\alpha_x^2} |G_x| e^{-i(\Omega_{rf} t + \tan^{-1}\alpha_x + \phi_x)}] \\ & + \frac{E_{0y}}{2} e^{i\omega_c t}\, e^{i\phi_{0y}} [2\cos\Delta\phi_{0y} \\ & + \frac{m_y V_0 \sin\Delta\phi_{0y}}{2} \sqrt{1+\alpha_y^2} |G_y| e^{-i(\Omega_{rf} t + \tan^{-1}\alpha_y + \phi_y)}], \end{aligned} \quad (4)$$

where

$$|G_{x,y}(\omega_c - \Omega_{rf})| = \exp\left\{ -\frac{\frac{g_{x,y}}{2}}{1 + 4\left[\frac{\omega_p - (\omega_c - \Omega_{rf}) + \Omega_{B_{x,y}}}{\Gamma_B}\right]^2} \right\}, \quad (5)$$

and

$$\phi_{x,y}(\omega_c - \Omega_{rf}) = \frac{g_{x,y}\left[\frac{\omega_p - (\omega_c - \Omega_{rf}) + \Omega_{B_{x,y}}}{\Gamma_B}\right]}{1 + 4\left[\frac{\omega_p - (\omega_c - \Omega_{rf}) + \Omega_{B_{x,y}}}{\Gamma_B}\right]^2}. \quad (6)$$

Here, $G_{x,y}$ and $\phi_{x,y}$ are the Brillouin loss and SBS-induced phase, respectively, as experienced by orthogonal

polarization components of the probe sideband at a radio frequency of $\Omega_{\rm rf}$. Γ_B is the Brillouin linewidth and $\Omega_{B_{x,y}}$ are the Brillouin resonance frequencies for x and y polarizations. The gain exponent, $g_{x,y}$, for the x and y polarizations of the probe sideband is related to the effective length, $L_{\rm eff}$; pump mode area, $A_{\rm eff}$; and Brillouin gain coefficient, g_B, by $g_{x,y} = g_B P^p_{x,y} L_{\rm eff}/A_{\rm eff}$, where $P^p_{x,y}$ is the pump power coupled along the x and y polarizations of the pump. The rf power, $S(\Omega_{\rm rf})$, at the photodetector is then obtained according to [57]

$$S(\Omega_{\rm rf}) = A_x|G_x|^2 + A_y|G_y|^2 + 2\sqrt{(A_x A_y)}\,|G_x||G_y|\cos(\tan^{-1}\alpha_x - \tan^{-1}\alpha_y - \phi_x + \phi_y), \tag{7}$$

where $A_{x,y} = I^2_{0x,0y}\sin^2\Delta\phi_{x,y} m^2_{x,y}(1+\alpha^2_{x,y})\kappa^2 R_L/64$, κ is the detector responsivity, R_L is the load resistance, and $I_{0x,0y} = |E_{0x,0y}|^2$. Destructive interference between the two Brillouin loss resonances in the rf domain occurs at a radio frequency of $\Omega_{\rm rf}$ (see Fig. 1, node f), for which $P_x^{\Omega_{\rm rf}} = P_y^{\Omega_{\rm rf}}$ and $\Phi_{x-y}^{\Omega_{\rm rf}} = (\tan^{-1}\alpha_x - \tan^{-1}\alpha_y - \phi_x + \phi_y) = \pi$, where $P_x^{\Omega_{\rm rf}}$ and $P_y^{\Omega_{\rm rf}}$ are the rf powers of the x- and y-polarized probe components [see Fig. 2(a)], and $\Phi_{x-y}^{\Omega_{\rm rf}}$ is the phase difference between them. We achieve a π phase shift between the interfering rf signals at the radio frequency for which their amplitudes are equal by tuning the bias-controlled rf phase. Outside the Brillouin loss bandwidth, even though the phase difference between the interfering rf signals is close to π, a large difference between the rf powers does not cause any destructive interference (see Fig. 2).

Figure 2 shows the simulation results for the EIA-based MPNF using the model developed above. Figure 2(a) plots the rf powers ($P_{\rm rf}$) for the x- (red dashed-dotted line) and y-polarized (black solid line) probe components, where both powers are normalized with respect to y polarization. Outside the Brillouin loss bandwidth, the rf power of the y-polarized probe is about 10 dB higher than the x-polarized probe component. Within the Brillouin loss bandwidth, the rf powers of the x- and y-polarized probe components are equalized at the desired frequency by tuning the pump polarization to create a large loss for the y polarization and a small loss at the x-polarized modulation sideband [see Fig. 2(a)]. The Brillouin-induced optical phases, $\phi_{x,y}$, for the interfering rf signals depend on the pump power along the respective polarization. The pump power along each polarization component is determined by the Brillouin loss required to equalize their rf powers at the desired frequency, which limits tuning of the optical phases, $\phi_{x,y}$. However, the electrically controlled phases, $\tan^{-1}\alpha_x$ and $\tan^{-1}\alpha_y$, for the x and y polarization, respectively, can be tuned by varying the bias voltage to the intensity modulator. The simulated rf phase response for the x- and y-polarized probe components is plotted in Fig. 2(b). By tuning the bias voltage, one can tune the values of $\alpha_{x,y}$ to create a π phase shift between the interfering signals at the frequency for which their amplitudes are equalized, as shown in Fig. 2(b). Furthermore, we see from Fig. 2(b) that the optically induced phase is smaller for the probe component that sees lower Brillouin loss, as expected according to Eq. (4). Equal amplitude and a π phase difference then enhance the loss through destructive interference between the interfering signals [see Fig. 2(c)], which results in a large rejection band via an analogue of EIA. Figure 2(d) shows the simulated phase response of the MPNF, which

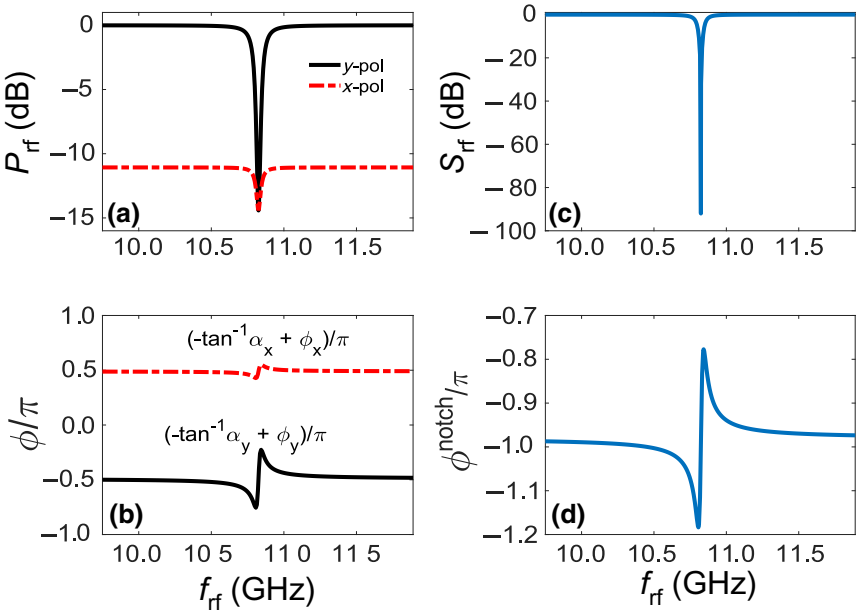

FIG. 2. Simulation results for concept of MPNF. (a) Normalized rf response ($P_{\rm rf}$) of x- (red dashed-dotted line) and y-polarized (black solid line) probe components. Both plots are normalized with respect to y-polarization power. (b) The rf-phase responses of individual polarization components. (c) Normalized rf response ($S_{\rm rf}$) of the MPNF, demonstrating Brillouin loss enhancement due to the analogue of EIA. (d) Simulated rf-phase response of the MPNF.

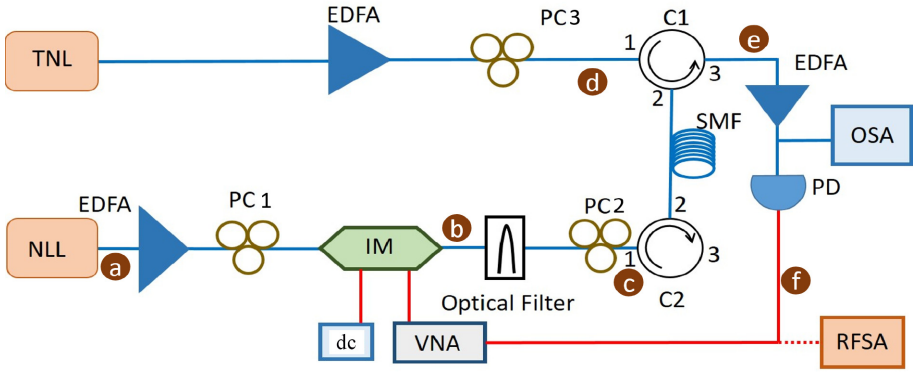

FIG. 3. Experimental setup for the demonstration of EIA-based MPNF. NLL, narrow-linewidth laser; TNL, tunable narrow-linewidth laser; EDFA, erbium-doped fiber amplifier; SMF, single-mode fiber; PC, polarization controller; VNA, vector network analyzer; PD, photodetector; RFSA, rf spectrum analyzer; OSA, optical spectrum analyzer; C1 and C2 are circulators 1 and 2, respectively.

is obtained from the phase difference between x- and y-polarized probe components. From Figs. 2(a) and 2(c), we infer that the large amplitude difference between the interfering components outside the loss bandwidth prevents destructive interference, even though they have a π phase difference, and thus, does not introduce any rf loss.

III. EXPERIMENTAL RESULTS AND DISCUSSION

Figure 3 shows the experimental setup for the EIA-based MPNF. Nodes labeled (a)–(f) in Fig. 3 correspond to the respective nodes in Fig. 1. Light from a NLL (∼5 kHz) centered at 1550 nm is amplified using an EDFA, which acts as the optical carrier. The amplified signal is then modulated with the desired radio frequency ($\Omega_{\rm rf}$) from a VNA using a z-cut IM. The bias port of the IM is connected to a tunable dc source. PC1 is used before the intensity modulator to feed the modulator with both polarization components to control their phase using V_b. The upper modulation sideband of the modulated signal ($\omega_C + \Omega_{\rm rf}$) is filtered out using a fiber Bragg grating (FBG) based narrowband optical filter to create a probe consisting of a single-modulation sideband ($\omega_C - \Omega_{\rm rf}$) and a laser carrier ($\omega_C$). Light from a TNL (∼1 kHz) is optically amplified using a high-power EDFA to create the Brillouin pump at a frequency of $\omega_c - \Omega_{\rm rf} - \Omega_B$. Pump and probe powers along the orthogonal polarization components are controlled using PC3 and PC2 in the respective arms. The probe signal and the Brillouin pump are allowed to interact in a 500-m-long SMF using C1 and C2. The Brillouin loss seen by each polarization component of the probe's modulation sideband depends on the pump power coupled along that polarization. The probe signal is collected at the third port of C1 and amplified using a low-noise EDFA. The output signal of the EDFA is allowed to beat on an ultrafast PD (Finisar) to down convert the modulated signal. A VNA and a RFSA are used after the PD to measure the rf response and to perform the resolution study. To measure

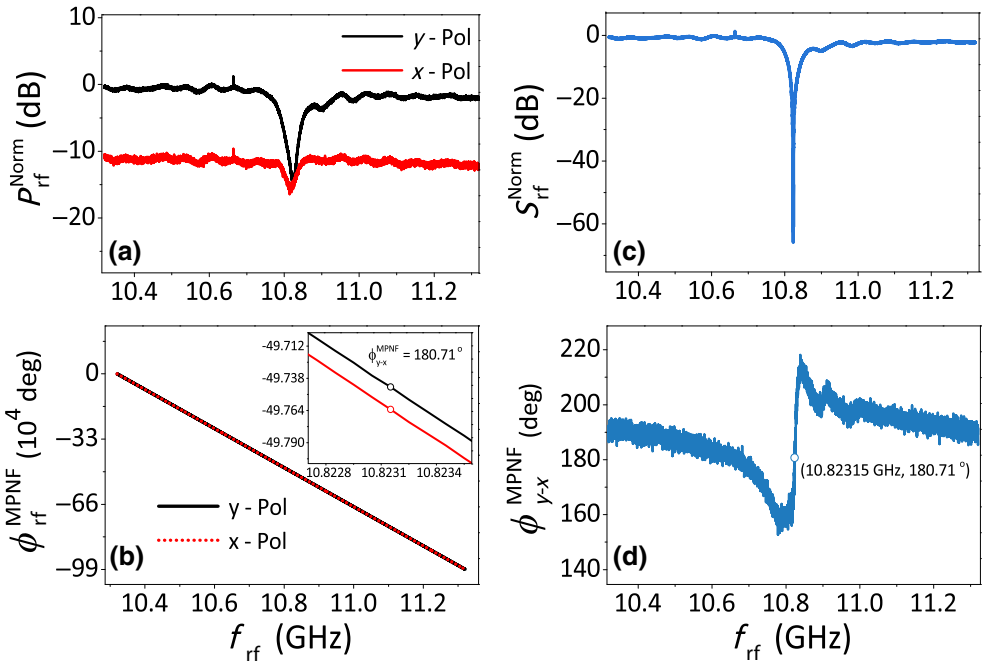

FIG. 4. Measured concept of EIA-based MPNF. (a) Normalized rf responses of x (red) and y (black) polarizations. (b) The rf phase responses of individual polarizations. Inset plots a magnified version of the rf phase for the two polarizations, showing that a π shift is achieved at the MPNF frequency. (c) Normalized rf response of the MPNF. (d) The rf phase response of the MPNF.

the rf response for the individual polarization components in Figs. 4(a) and 4(b), a polarization beam splitter is used before the PD.

Figure 4(a) shows the rf response for the x- (red solid line) and y-polarized (black solid line) probe components normalized with respect to the measured y-polarization component. By tuning PC2 in the probe arm, we control the rf power distribution in the individual polarization components of the probe to create an amplitude imbalance of about 10 dB between beat signals. The rf response for each polarization is measured using a polarization beam splitter before the photodetector. The rf powers of the probe polarization components are equalized at the desired radio frequency [see Fig. 4(a)] by tuning the pump polarization (PC3) to control the Brillouin loss seen by them. The rf phase measurements for the x- and y-polarized probe components are shown in Fig. 4(b). The bias voltage of the IM is tuned in such a way that the phase difference between the polarization components become π at the radio frequency where their amplitudes are equalized. Inset in Fig. 4(b) shows that a phase difference of π occurs at the desired frequency. These conditions then result in destructive interference between the two rf absorption features, as shown in Fig. 4(a), which drastically enhances signal rejection and results in the EIA-based MPNF response shown in Fig. 4(c). The measured phase response of the MPNF is shown in Fig. 4(d), which is obtained by calculating the difference between the rf phases of the x and y polarizations shown in Fig. 4(b). The notch filter is realized at a frequency of 10.823 GHz within the Brillouin loss resonance, where the phase difference is equal to 180.71°. From Figs. 4(a) and 4(c), we note that we realize a rf loss resonance of about 70 dB using a total Brillouin loss of only about 19 dB. In a conventional SBS MPNF based on SSB modulation, a notch depth of 70 dB would require a Brillouin loss of 70 dB. We, therefore, present a highly efficient MPNF using the SSB modulation scheme.

Figures 5(a)–5(i) show the S_{21} measurements for the EIA-based MPNF over a wide frequency range of 4–40 GHz. The modulation frequency (Ω_{rf}) of the probe's intensity modulator is tuned from 4 to 40 GHz and, accordingly, the Brillouin pump frequency is tuned to generate the SBS loss resonance. For the entire tuning range, we achieve an ultrahigh rejection of $>$ 75 dB using a SBS loss of about 15 dB, which corresponds to a loss enhancement of $>$ 60 dB. Such a large notch response using a low SBS loss with

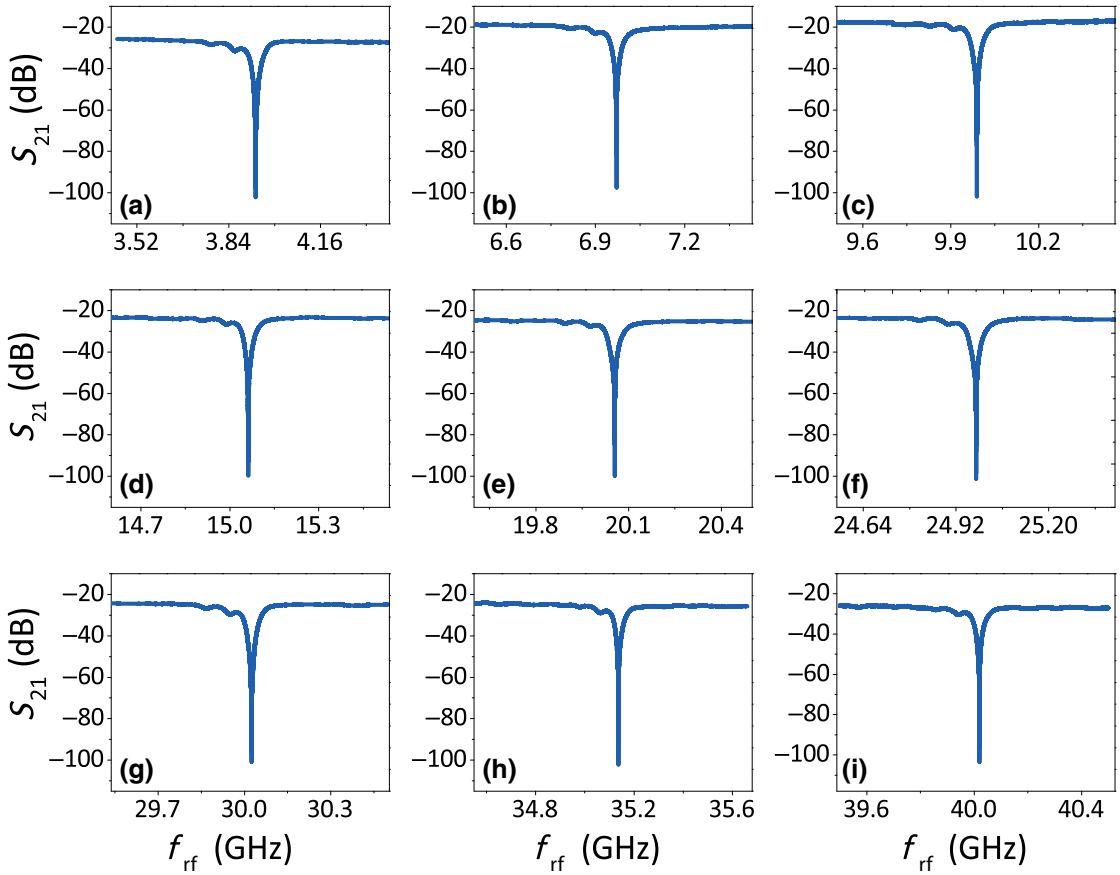

FIG. 5. Wideband study of MPNF. (a)–(i) Measured MPNF responses (S_{21}) up to 40 GHz. Throughout the tuning range, the MPNF achieves a record notch depth of >75 dB, while keeping the rf loss at (22.9 ± 5.4) dB.

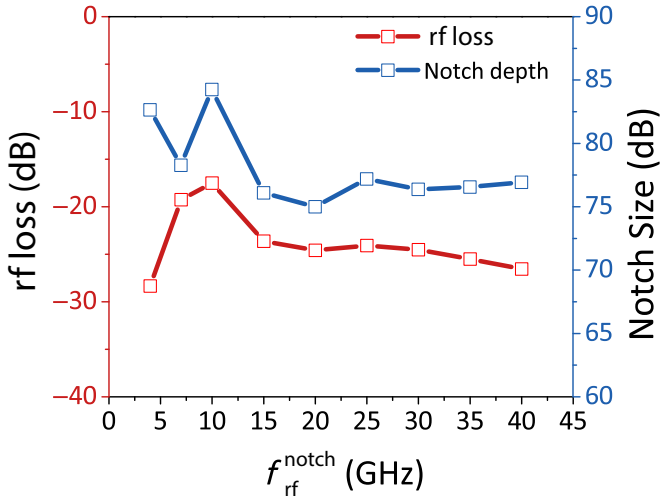

FIG. 6. Measured rf loss (red) and rejection depth (blue) for different notch frequencies.

the SSB modulation scheme creates an efficient MPNF. Furthermore, the use of single-sideband modulation in our technique makes it less prone to dispersion-induced phase shifts, which reduce the notch depth [56]. In our scheme, fine control over the polarization components allows effective equalization of rf powers at the desired frequency. The bias control over the rf phases of the two polarizations allows fine-tuning of the phase to achieve the condition for destructive interference. By fitting Lorentzian profiles to the measured MPNF response in Figs. 5(a)–5(i), we obtain a narrow 3-dB bandwidth of (77 ± 7) MHz over the entire tuning range.

Figure 6 plots the notch size and rf loss for each notch frequency in Fig. 5. Over the entire tuning range, we achieve a rejection depth of > 75 dB, while maintaining a rf insertion loss of (-22.9 ± 5.4) dB. Here, the rf loss shows the total loss experienced by the signal when it passes through the experimental setup due to the insertion losses of the individual components. The z-cut intensity modulator shows an insertion loss of about 10 to 29 dB, when the modulation frequency changes from 1 to 40 GHz, which causes a similar frequency dependence of the insertion loss in our MPNF. At low frequencies, the modulation sidebands are close to the carrier, so a portion of the carrier is suppressed by the optical filter that is used for filtering the upper modulation sideband. The reduction in carrier power due to the optical filter results in a lower rf power at the photodetector, and thus, higher insertion loss at small frequencies. These losses can be reduced using a high-bandwidth modulator, using photonic components with low-loss and high-power handling, and replacing the optical filter with one having a narrower bandwidth [18,64]. We realize a minimum rf loss of about 17.5 dB at 10 GHz. For the entire frequency range, we use a Brillouin loss of about 15 dB.

To demonstrate the effectiveness of the EIA-based MPNF, we perform a resolution study, where we suppress an unwanted interferer in the presence of a rf signal. We create an interferer and signal using two rf tones with 70-MHz frequency difference. Figures 7(a) and 7(b) show the system with both an interferer and the desired rf signal measured after the photodetector when the Brillouin pump is off and Brillouin pump is on, respectively. Since both measurements are performed after the photodetector, the insertion loss is already incorporated. The power of the interferer is kept 25 dB higher than the signal, as shown in Fig. 7(a), which shows only the passband response of the system because the Brillouin pump is off. In the presence of the Brillouin pump, the orthogonally polarized probe components experience different SBS losses and equalize the powers at the interferer frequency, which results in a notch-filter response that leads to the suppression of the unwanted interferer. Here, the interferer experiences 51-dB suppression, while the signal in the passband remains unaffected

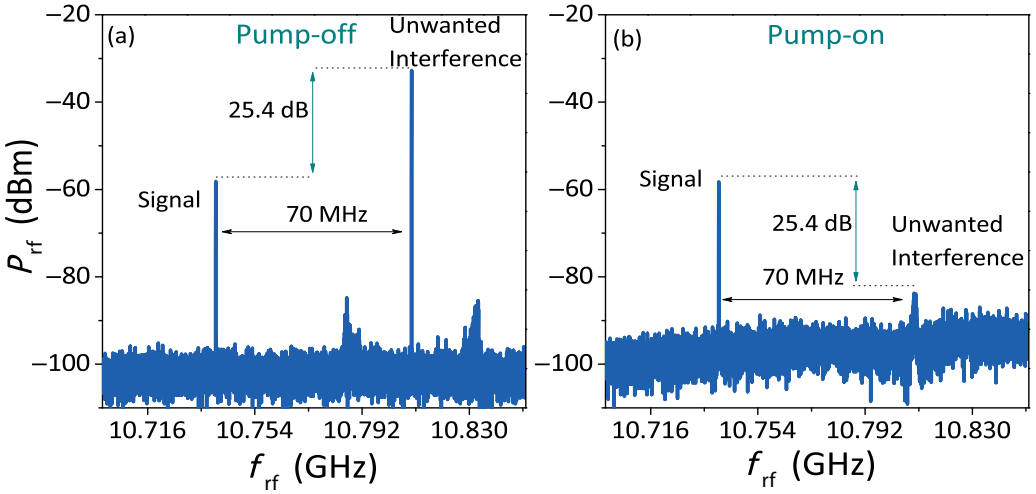

FIG. 7. Filtering of a strong unwanted interferer placed 70 MHz apart from desired signal. (a) System when the pump is off, showing that the unwanted interferer is 25.4 dB stronger than the desired rf signal. (b) System when the pump is on, where the unwanted interferer is suppressed by 50.8 dB, while the signal remains unaffected.

TABLE I. Comparison of different MPNF techniques. In the rf gain column, negative and positive signs represent loss and gain, respectively. MZM, Mach-Zehnder modulator; PM, phase modulator; MRR, microring resonator; SOI, silicon on insulator.

Technique	Rejection (dB)	Tunability (GHz)	Bandwidth (MHz)	rf gain (dB)	Modulation format
This work	> 75	4–40	77 ± 7	-22.9 ± 5.4	SSB
Photonic crystal [16]	> 50	10–50	1000	-45	DSB
Silicon nitride chip [18]	50	0–12	150	$+8$	DSB
MRRs on a single SOI [20]	40	2.5–17.5	6000–9500	...	DSB
Silicon MRR [22]	> 60	12.4–30.6	...	...	DSB
PM-incorporated Lyot filter [29]	> 60	1.8–10	820–1800 (10 dB)	< -30	SSB
SBS + MZM[54]	40	2–20	82	...	DSB
SBS loss [46]	20	2–8	126	> -10	SSB
DSB + SBS gain or loss [47]	> 60	1–30	10	...	DSB
SBS + polarization conversion [41]	67	3–5	64	...	SSB
Two SSB signals [65]	0–40 (tunable)	1.5–6.5	180	< -30	SSB
DSB + SBS loss and gain [53]	> 65	1–25	50	-14	DSB

[see Fig. 7(b)]. The technique, therefore, provides a high-resolution large-extinction MPNF using SSB modulation and low Brillouin loss.

IV. CONCLUSION

We exploit destructive interference between Brillouin loss resonances, created by orthogonally polarized probe components in the rf domain, to enhance Brillouin loss by more than 6 orders of magnitude. We harness this analogue of EIA within Brillouin loss to demonstrate an efficient MPNF with an ultrahigh rejection of > 75 dB using a Brillouin loss of about 15 dB. Over the entire tuning range of 4–40 GHz, we achieve a rf gain of (-22.9 ± 5.4) dB. A maximum notch depth of 84 dB is observed at 10 GHz. The proposed MPNF exhibits a narrow 3-dB linewidth of (77 ± 7) MHz over the entire 40-GHz frequency range. Furthermore, the use of single-sideband modulation reduces the effect of dispersion-induced phase detuning from π at the destructive-interference frequency.

While MPNFs with > 60-dB rejection are demonstrated over a wide-frequency range using a combination of rf interference and DSB modulation (see Table I), the notch depth in single-sideband-modulation-based MPNFs is limited due to the requirement of large Brillouin loss or passive resonators with a large extinction. Our demonstration, which uses a total Brillouin loss of about 15 dB to realize a MPNF with > 75-dB rejection, presents a highly efficient MPNF using SSB modulation. Brillouin scattering and other photonic components, such as FBG or intensity modulator, as used in our demonstration, are realized on a photonic chip [66–71]. The EIA-based MPNF, therefore, has the potential to realize a highly efficient MPNF with ultrahigh rejection.

ACKNOWLEDGMENTS

We wish to acknowledge funding support from the Science and Engineering Research Board (SERB), the Department of Science and Technology (DST) through a Ramanujan Fellowship (Grant No. SB/S2/RJN-069/2014), and the University Grand Commission (UGC) through a JRF-NET fellowship.

[1] S. Gertler, E. A. Kittlaus, N. T. Otterstrom, P. Kharel, and P. T. Rakich, Microwave filtering using forward Brillouin scattering in photonic–phononic emit-receive devices, J. Light. Technol. **38**, 5248 (2020).

[2] E. A. Kittlaus, P. Kharel, N. T. Otterstrom, Z. Wang, and P. T. Rakich, Rf-photonic filters via on-chip photonic–phononic emit-receive operations, J. Light. Technol. **36**, 2803 (2018).

[3] J. Li, H. Lee, and K. J. Vahala, Microwave synthesizer using an on-chip Brillouin oscillator, Nat. Commun. **4**, 1 (2013).

[4] J. Li, X. Yi, H. Lee, S. A. Diddams, and K. J. Vahala, Electro-optical frequency division and stable microwave synthesis, Science **345**, 309 (2014).

[5] R. Pant, D. Marpaung, I. V. Kabakova, B. Morrison, C. G. Poulton, and B. J. Eggleton, On-chip stimulated Brillouin scattering for microwave signal processing and generation, Laser Photonics Rev. **8**, 653 (2014).

[6] D. Marpaung, C. Roeloffzen, R. Heideman, A. Leinse, S. Sales, and J. Capmany, Integrated microwave photonics, Laser Photonics Rev. **7**, 506 (2013).

[7] D. Marpaung, J. Yao, and J. Capmany, Integrated microwave photonics, Nat. Photonics **13**, 80 (2019).

[8] J. Hervás, A. L. Ricchiuti, W. Li, N. H. Zhu, C. R. Fernández-Pousa, S. Sales, M. Li, and J. Capmany, Microwave photonics for optical sensors, IEEE J. Sel. Top. Quantum Electron. **23**, 327 (2017).

[9] J. Yao, Microwave photonics, J. Light. Technol. **27**, 314 (2009).

[10] J. Capmany and D. Novak, Microwave photonics combines two worlds, Nat. Photonics **1**, 319 (2007).

[11] D. Marpaung, M. Pagani, B. Morrison, and B. J. Eggleton, Nonlinear integrated microwave photonics, J. Light. Technol. **32**, 3421 (2014).

[12] G. S. Wiederhecker, P. Dainese, and T. P. Mayer Alegre, Brillouin optomechanics in nanophotonic structures, APL Photonics **4**, 071101 (2019).
[13] J. Wang and J. Yao, A tunable photonic microwave notch filter based on all-optical mixing, IEEE Photon Technol. Lett. **18**, 382 (2006).
[14] E. H. W. Chan and R. A. Minasian, High-resolution tunable RF/microwave photonic notch filter with low-noise performance, J. Light. Technol. **29**, 3304 (2011).
[15] V. Supradeepa, C. M. Long, R. Wu, F. Ferdous, E. Hamidi, D. E. Leaird, and A. M. Weiner, Comb-based radiofrequency photonic filters with rapid tunability and high selectivity, Nat. Photonics **6**, 186 (2012).
[16] J. Sancho, J. Bourderionnet, J. Lloret, S. Combrié, I. Gasulla, S. Xavier, S. Sales, P. Colman, G. Lehoucq, and D. Dolfi, *et al.*, Integrable microwave filter based on a photonic crystal delay line, Nat. Commun. **3**, 1 (2012).
[17] V. Polo, B. Vidal, J. Corral, and J. Marti, Novel tunable photonic microwave filter based on laser arrays and N/spl times/N AWG-based delay lines, IEEE Photon Technol. Lett. **15**, 584 (2003).
[18] Y. Liu, J. Hotten, A. Choudhary, B. J. Eggleton, and D. Marpaung, All-optimized integrated RF photonic notch filter, Opt. Lett. **42**, 4631 (2017).
[19] M. S. Rasras, K.-Y. Tu, D. M. Gill, Y.-K. Chen, A. White, S. Patel, A. Pomerene, D. Carothers, J. Beattie, M. Beals, J. Michel, and L. Kimerling, Demonstration of a tunable microwave-photonic notch filter using low-loss silicon ring resonators, J. Light. Technol. **27**, 2105 (2009).
[20] J. Dong, L. Liu, D. Gao, Y. Yu, A. Zheng, T. Yang, and X. Zhang, Compact notch microwave photonic filters using on-chip integrated microring resonators, IEEE Photonics J. **5**, 5500307 (2013).
[21] D. Marpaung, B. Morrison, R. Pant, C. Roeloffzen, A. Leinse, M. Hoekman, R. Heideman, and B. J. Eggleton, Si3N4 ring resonator-based microwave photonic notch filter with an ultrahigh peak rejection, Opt. Express **21**, 23286 (2013).
[22] Y. Long and J. Wang, Ultra-high peak rejection notch microwave photonic filter using a single silicon microring resonator, Opt. Express **23**, 17739 (2015).
[23] B. Yu, Y. Chen, J. Pan, B. Zhang, F. Li, L. Wan, X. Guo, J. Li, and Z. Li, Silica-microsphere-cavity-based microwave photonic notch filter with ultra-narrow bandwidth and high peak rejection, Opt. Lett. **44**, 1411 (2019).
[24] O. Daulay, G. Liu, and D. Marpaung, Microwave photonic notch filter with integrated phase-to-intensity modulation transformation and optical carrier suppression, Opt. Lett. **46**, 488 (2021).
[25] P. Zheng, H. Hong, J. Li, G. Hu, B. Yun, and Y. Cui, Performances of microwave photonic notch filter based on microring resonator with dual-drive modulator, IEEE Photonics J. **11**, 1 (2019).
[26] Y. Liu, D. Marpaung, A. Choudhary, J. Hotten, and B. J. Eggleton, Link performance optimization of chip-based Si3N4 microwave photonic filters, J. Light Technol. **36**, 4361 (2018).
[27] E. H. W. Chan and R. A. Minasian, Widely tunable, high-FSR, coherence-free microwave photonic notch filter, J. Light Technol. **26**, 922 (2008).
[28] E. Chan and R. Minasian, Sagnac-loop-based equivalent negative tap photonic notch filter, IEEE Photon Technol. Lett. **17**, 1740 (2005).
[29] J. Ge, H. Feng, G. Scott, and M. P. Fok, High-speed tunable microwave photonic notch filter based on phase modulator incorporated Lyot filter, Opt. Lett. **40**, 48 (2015).
[30] D. Pastor, J. Capmany, and B. Ortega, Broad-band tunable microwave transversal notch filter based on tunable uniform fiber Bragg gratings as slicing filters, IEEE Photon Technol. Lett. **13**, 726 (2001).
[31] X. Xu, M. Tan, J. Wu, T. G. Nguyen, S. T. Chu, B. E. Little, R. Morandotti, A. Mitchell, and D. J. Moss, High performance RF filters via bandwidth scaling with kerr micro-combs, APL Photonics **4**, 026102 (2019).
[32] R. W. Boyd, in *Nonlinear Optics*, edited by R. W. Boyd (Academic Press, San Diego, 2003), 2nd ed., p. 409.
[33] G. Agrawal, in *Nonlinear Fiber Optics*, edited by G. Agrawal, Optics and Photonics (Academic Press, Boston, 2013), 5th ed., p. 353.
[34] E. A. Kittlaus, N. T. Otterstrom, and P. T. Rakich, On-chip inter-modal Brillouin scattering, Nat. Commun. **8**, 1 (2017).
[35] H. Shin, W. Qiu, R. Jarecki, J. A. Cox, R. H. Olsson, A. Starbuck, Z. Wang, and P. T. Rakich, Tailorable stimulated Brillouin scattering in nanoscale silicon waveguides, Nat. Commun. **4**, 1 (2013).
[36] B. J. Eggleton, C. G. Poulton, and R. Pant, Inducing and harnessing stimulated Brillouin scattering in photonic integrated circuits, Adv. Opt. Photon **5**, 536 (2013).
[37] S. Gertler, E. A. Kittlaus, N. T. Otterstrom, and P. T. Rakich, Tunable microwave-photonic filtering with high out-of-band rejection in silicon, APL Photonics **5**, 096103 (2020).
[38] A. Byrnes, R. Pant, E. Li, D.-Y. Choi, C. G. Poulton, S. Fan, S. Madden, B. Luther-Davies, and B. J. Eggleton, Photonic chip based tunable and reconfigurable narrowband microwave photonic filter using stimulated Brillouin scattering, Opt. Express **20**, 18836 (2012).
[39] C. Feng, S. Preussler, and T. Schneider, Sharp tunable and additional noise-free optical filter based on Brillouin losses, Photon Res. **6**, 132 (2018).
[40] A. Wise, M. Tur, and A. Zadok, Sharp tunable optical filters based on the polarization attributes of stimulated Brillouin scattering, Opt. Express **19**, 21945 (2011).
[41] G. Zoireff, D. Samaniego, and B. Vidal, Dynamic filtering of microwave signals through Brillouin-based polarization-sensitive balanced detection, IEEE J. Sel. Top. Quantum Electron. **27**, 1 (2021).
[42] B. Vidal, M. A. Piqueras, and J. Martí, Tunable and reconfigurable photonic microwave filter based on stimulated Brillouin scattering, Opt. Lett. **32**, 23 (2007).
[43] W. Zhang and R. A. Minasian, Widely tunable single-passband microwave photonic filter based on stimulated Brillouin scattering, IEEE Photon Technol. Lett. **23**, 1775 (2011).
[44] Y. Stern, K. Zhong, T. Schneider, R. Zhang, Y. Ben-Ezra, M. Tur, and A. Zadok, Tunable sharp and highly selective microwave-photonic band-pass filters based on stimulated Brillouin scattering, Photon Res. **2**, B18 (2014).
[45] A. Mahendra, Y. Liu, E. Magi, A. Choudhary, D. Marpaung, and B. J. Eggleton, High link performance of

Brillouin-loss based microwave bandpass photonic filters, OSA Contin. **1**, 1287 (2018).

[46] B. Morrison, D. Marpaung, R. Pant, E. Li, D.-Y. Choi, S. Madden, B. Luther-Davies, and B. J. Eggleton, Tunable microwave photonic notch filter using on-chip stimulated Brillouin scattering, Opt. Commun. **313**, 85 (2014).

[47] D. Marpaung, B. Morrison, R. Pant, and B. J. Eggleton, Frequency agile microwave photonic notch filter with anomalously high stopband rejection, Opt. Lett. **38**, 4300 (2013).

[48] W. Zhang and R. A. Minasian, Switchable and tunable microwave photonic Brillouin-based filter, IEEE Photonics J. **4**, 1443 (2012).

[49] D. Marpaung, B. Morrison, M. Pagani, R. Pant, D.-Y. Choi, B. Luther-Davies, S. J. Madden, and B. J. Eggleton, Low-power, chip-based stimulated Brillouin scattering microwave photonic filter with ultrahigh selectivity, Optica **2**, 76 (2015).

[50] Y. Liu, D. Marpaung, A. Choudhary, and B. J. Eggleton, Lossless and high-resolution RF photonic notch filter, Opt. Lett. **41**, 5306 (2016).

[51] Y. Liu, A. Choudhary, G. Ren, K. Vu, B. Morrison, A. Casas-Bedoya, T. G. Nguyen, D.-Y. Choi, P. Ma, A. Mitchell, S. J. Madden, D. Marpaung, and B. J. Eggleton, Integration of Brillouin and passive circuits for enhanced radio-frequency photonic filtering, APL Photonics **4**, 106103 (2019).

[52] S. Chin, L. Thévenaz, J. Sancho, S. Sales, J. Capmany, P. Berger, J. Bourderionnet, and D. Dolfi, Broadband true time delay for microwave signal processing, using slow light based on stimulated Brillouin scattering in optical fibers, Opt. Express **18**, 22599 (2010).

[53] A. Siva Shakthi, M. K. Varun, and R. Pant, Dynamic dispersion compensation for wideband microwave photonic notch filter with high rejection and high-resolution, IEEE J. Sel. Top. Quantum Electron. **27**, 1 (2021).

[54] W. Zhang and R. A. Minasian, Ultrawide tunable microwave photonic notch filter based on stimulated Brillouin scattering, IEEE Photon Technol. Lett. **24**, 1182 (2012).

[55] A. Casas-Bedoya, B. Morrison, M. Pagani, D. Marpaung, and B. J. Eggleton, Tunable narrowband microwave photonic filter created by stimulated Brillouin scattering from a silicon nanowire, Opt. Lett. **40**, 4154 (2015).

[56] C. Feng, S. Preussler, and T. Schneider, The influence of dispersion on stimulated-Brillouin-scattering-based microwave photonic notch filters, J. Light Technol. **36**, 5145 (2018).

[57] A. Siva Shakthi, A. B. Yelikar, and R. Pant, Analogue of electromagnetically induced absorption in the microwave domain using stimulated Brillouin scattering, Commun. Phys. **3**, 1 (2020).

[58] X. Zhang, N. Xu, K. Qu, Z. Tian, R. Singh, J. Han, G. S. Agarwal, and W. Zhang, Electromagnetically induced absorption in a three-resonator metasurface system, Sci. Rep. **5**, 1 (2015).

[59] R. Taubert, M. Hentschel, J. Kästel, and H. Giessen, Classical analog of electromagnetically induced absorption in plasmonics, Nano Lett. **12**, 1367 (2012).

[60] D. Floess, M. Hentschel, T. Weiss, H.-U. Habermeier, J. Jiao, S. G. Tikhodeev, and H. Giessen, Plasmonic Analog of Electromagnetically Induced Absorption Leads to Giant Thin Film Faraday Rotation of 14, Phys. Rev. X **7**, 021048 (2017).

[61] P. Tassin, L. Zhang, R. Zhao, A. Jain, T. Koschny, and C. M. Soukoulis, Electromagnetically Induced Transparency and Absorption in Metamaterials: The Radiating Two-Oscillator Model and its Experimental Confirmation, Phys. Rev. Lett. **109**, 187401 (2012).

[62] T. Dennis and P. A. Williams, Chirp characterization of external modulators with finite extinction ratio using linear optical sampling, IEEE Photon Technol. Lett. **22**, 646 (2010).

[63] C. E. Rogers, III, J. L. Carini, J. A. Pechkis, and P. L. Gould, Characterization and compensation of the residual chirp in a Mach-Zehnder-type electro-optical intensity modulator, Opt. Express **18**, 1166 (2010).

[64] H. Zhu, R. Wang, P. Xiang, T. Pu, J. Zheng, Y. Li, T. Fang, L. Huang, Y. Han, and X. Chen, Microwave photonic bandpass filter based on carrier-suppressed single sideband injected distributed feedback laser, IEEE Photonics J. **9**, 1 (2017).

[65] E. Xu and J. Yao, Frequency- and notch-depth-tunable single-notch microwave photonic filter, IEEE Photon Technol. Lett. **27**, 2063 (2015).

[66] R. Pant, C. G. Poulton, D.-Y. Choi, H. Mcfarlane, S. Hile, E. Li, L. Thevenaz, B. Luther-Davies, S. J. Madden, and B. J. Eggleton, On-chip stimulated Brillouin scattering, Opt. Express **19**, 8285 (2011).

[67] W. M. J. Green, M. J. Rooks, L. Sekaric, and Y. A. Vlasov, Ultra-compact, low RF power, 10 Gb/s silicon Mach-Zehnder modulator, Opt. Express **15**, 17106 (2007).

[68] S. Gundavarapu, G. M. Brodnik, M. Puckett, T. Huffman, D. Bose, R. Behunin, J. Wu, T. Qiu, C. Pinho, and N. Chauhan, *et al.*, Sub-hertz fundamental linewidth photonic integrated Brillouin laser, Nat. Photonics **13**, 60 (2019).

[69] L. Agazzi, J. D. B. Bradley, M. Dijkstra, F. Ay, G. Roelkens, R. Baets, K. Wörhoff, and M. Pollnau, Monolithic integration of erbium-doped amplifiers with silicon-on-insulator waveguides, Opt. Express **18**, 27703 (2010).

[70] W. Zhang and J. Yao, A fully reconfigurable waveguide Bragg grating for programmable photonic signal processing, Nat. Commun. **9**, 1 (2018).

[71] S. Assefa, F. Xia, and Y. A. Vlasov, Reinventing germanium avalanche photodetector for nanophotonic on-chip optical interconnects, Nature **464**, 80 (2010).